Splashing during impact on heated granular beds

Fangye Lin,[1,2] Yihua Yang,[3] Jun Zou,[1,2,*] and William D. Ristenpart[3,†]
[1]*Ningbo Research Institute, Zhejiang University, Ningbo 315048, China*
[2]*State Key Laboratory of Fluid Power and Mechatronic Systems, Zhejiang University, Hangzhou 310027, China*
[3]*Department of Chemical Engineering, University of California Davis, Davis, California 95616, USA*

(Received 29 April 2020; accepted 16 October 2020; published 9 November 2020)

We report that the splash created by a solid impactor moving into a bed of granular media depends sensitively on the temperature of the granular bed. Granules were poured loosely into an open-top container and then heated from below, and a metal ball was then dropped into the hot granular bed. High-speed video experiments reveal that the size and average velocity of the resulting granular splash both decrease significantly as the temperature increases. Complementary experiments show that the composition of the surrounding gas also strongly affects the splash dynamics but that the gas pressure and corresponding density have no significant effect. We interpret these observations in terms of two physical effects: the influence of the temperature- and composition-dependent gas viscosity on the ejecta drag force, and an enhanced static strength within the bed caused by thermal expansion of the granules. Taken together, the results indicate that temperature plays a greater role in granular splashing than previously suspected.

DOI: 10.1103/PhysRevFluids.5.114302

I. INTRODUCTION

When a solid object (such as a ball or marble) falls into a bed of solid-granular media (such as sand), the granules splash in a manner highly reminiscent of splashes formed by impacts into liquid media [1–3]. These granular splashes play an important role in sand and soil erosion processes [4,5], and at larger geophysical scales they help define the ejecta patterns resulting from meteorite strikes [6–9]. In contrast to liquid splashes, which have been studied extensively [10,11], the physics of granular splashing are less well understood. Previous work has established that the dynamics of the granular splash can be roughly classified into two stages: an acceleration stage of granules inside the granular bed, and a ballistic stage after the ejecta escape the bed. For a deep bed impact, Deboeuf *et al.* [12] hypothesized that all of the ejecta were suddenly accelerated at the same time but with a distribution of velocities. For a shallow layer impact, Boudet *et al.* [13] proposed that the acceleration of particles is first generated in the layer near the impact and then the disturbance travels horizontally and accelerates the nearby particles layers. Marston *et al.* [14] demonstrated that the compressibility of the granular material could suppress the propagation of the disturbance for short times following the impact, yielding a delay emergence of the ejecta.

Further work established that the interaction between the impactor and the granular material plays a key role. For a quicksand bed, the resistance applied to the impactor is related to the depth-dependent hydrostatic pressure [15,16] and the velocity-dependent inertial drag [17]. A major complicating factor for granular material involves the force chains [18] inside the bed, which are

*junzou@zju.edu.cn
†wdristenpart@ucdavis.edu

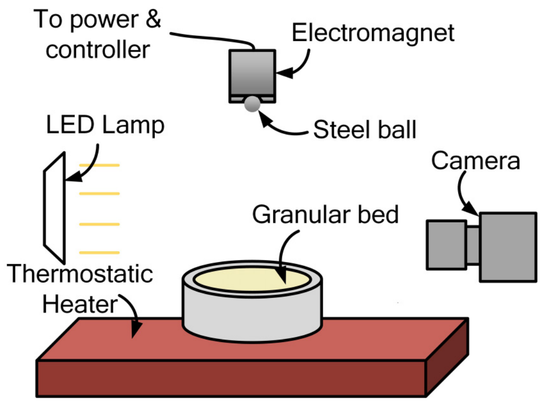

FIG. 1. Experimental setup. Setup for the tests of solid ball impact onto granular beds with varying temperature.

sensitive to the packing fraction ϕ [19] and also play a significant role in the overall resistance to acceleration. The resistance is also found related to the monodispersity of the bed that adding small particles to a bed of large sand particles may lead to a lubrication effect [20]. The ambient air pressure is also known to affect the granular dynamics. A higher air pressure was found to resist local compaction in the bed packing, thus hindering penetration of the impactor in a loose bed [21–24]. Caballero *et al.* suggested that the decrease in compaction is due to an extra sand fluidization caused by the air flow induced by the moving ball [22]. An alternative explanation proposed by Royer *et al.* posits that the interstitial air throughout the bed acts like a cushion, preventing the compaction of the bed at large pressures [1,23].

Notably, all of the above experimental studies of solid-granular impact were conducted at room temperature. None of the extant models include temperature, nor temperature-dependent physical properties such as the gas viscosity, as important parameters in predicting the splashing behavior. The main goal of this article is to report that temperature has a pronounced effect on granular splashing.

II. IMPACT ON HEATED GRANULAR BEDS

Our experimental apparatus included a heated bed containing a specified granular material, with a steel ball falling by gravity serving as the impactor (Fig. 1). The temperature of the bed was controlled by a thermostatic heater (Xinhaomai X200), while the steel ball (diameter 3.2 mm, weight 131 mg) was held by an electromagnet until release. The magnet was placed 150 mm above the surface of the granular bed, yielding an average impact velocity $U_b = 1.72\,\mathrm{m/s}$ with a standard deviation of 0.016 m/s [25]. This impactor mass and velocity were held constant in the experiments reported here, which focused on the effect of changing the granular bed temperature. Three types of commercial abrasive materials (silicon carbide, boron carbide, and aluminum oxide) with irregular (nonspherical) shape and various size were used in our experiments (Table I), chosen because they are chemically stable at high temperatures (less than 450 °C). We take the median diameter d_{50} (the value of the particle diameter at 50% in the cumulative distribution) as the characteristic diameter, i.e., $d_p = d_{50}$. The particles can be used here can be qualitatively classified into small size ($d_p \approx 50\ \mu$m), medium size ($d_p \approx 150\ \mu$m), and large size ($d_p \approx 230\ \mu$m). To conduct an experiment, the particles were poured into a hopper and allowed to fall freely into the cylindrical aluminum container (depth 10 mm, inner diameter 31 mm, wall thickness 2 mm, cf. Fig. 1). The top surface of the granular packing in the container was gently scraped with a glass slide to produce a uniform, level surface, and the bed was then heated to a target temperature by the thermostatic heater

TABLE I. Particle density, characteristic diameters, packing fraction, and repose angle for the seven granular materials tested here. The parameter d_k denotes the k th percentile for the particle size distribution.

	Small		Medium		Large		
Material	SiC	B_4C	SiC	B_4C	SiC	B_4C	Al_2O_3
ρ_p (kg/m^3)	3210	2520	3210	2540	3210	2540	3950
d_{10} (μm)	38	33	102	104	174	165	186
d_{50} (μm)	57	50	149	147	239	224	234
d_{90} (μm)	91	89	216	207	321	306	307
ϕ	0.39	0.45	0.46	0.46	0.52	0.50	0.46
θ (degrees)	35.7	34.1	34.1	34.3	35.3	35.9	37.0

for at least 30 min. The surface temperature of the bed T was measured by an infrared thermometer with an accuracy of $\pm 6\,^{\circ}$C. After the target temperature was obtained, the magnet was deactivated and the resulting granular splash was captured from the side by a high-speed camera (Phantom V7.3) at 2000 images per second. Backlighting was produced by a high-intensity light-emitting diode (LED) lamp (Maidnya 100 W) covered by an optical diffuser plate.

Representative splash dynamics for silicon carbide (Advanced Abrasives, $d_p = 57\,\mu$m) at different temperatures are shown in Fig. 2 (also see Supplemental Material, Video 1 [25]). At room temperature (Fig. 2, top row), the evolution of the splash is qualitatively similar to previous observations [12]. Upon impact, the solid ball pushed the granular particles away from the point of impact as the ball penetrated the granular layer. The particles accelerated to a high velocity and formed a corona (crown-shaped) splash, which expanded in size during the first 20–30 ms as the particles ejected away from the impact point. A pronounced granular jet also ejected vertically from near the center of the impact point, presumably caused by the collapse of the crater on itself [15,26]. The ejected particles then fell back, and the splash was largely finished (i.e., ejecta had landed and ceased motion) within 100 ms.

Holding all other parameters constant while increasing the temperature of the granular bed yielded qualitatively similar but increasingly "weaker" splashes (Fig. 2, middle and bottom rows). In contrast to the room-temperature impact, the splash at $T = 133\,^{\circ}$C exhibited a similar shape but yielded a clearly decreased amount of particles ejected into the air, with a smaller maximum height. The splash also dissipated more quickly; the majority of ejecta had landed by approximately $t = 50\,$ms. At the highest temperature tested of $T = 300\,^{\circ}$C (Fig. 2, bottom row), the splash

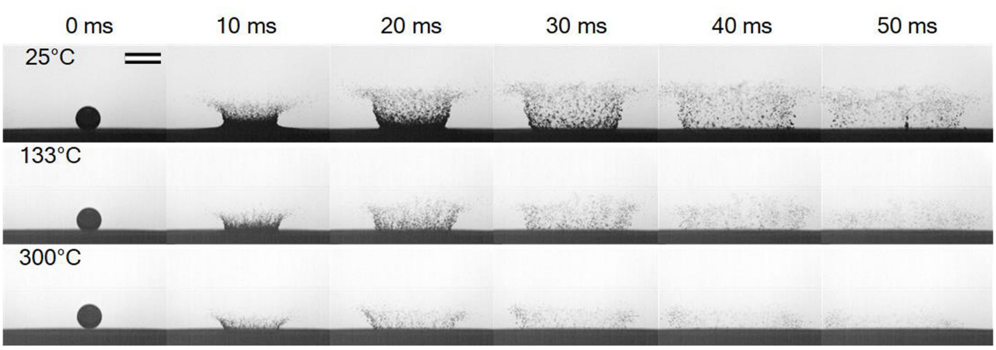

FIG. 2. The time evolution of the particle ejection after impact. The three rows (from top to bottom) represent impact at $T = 25\,^{\circ}$C, 133 °C, and 300 °C, respectively. The particles used here are SiC with $d_p = 57\,\mu$m. The impact velocity ($U_b = 1.72\,$m/s) is constant in all trials. Scale bar 5 mm.

was even more suppressed, with a clearly decreased maximum splash size that dissipated almost completely within 40 ms. No noticeable granular jets occurred at these higher temperatures.

To quantify these observations we used standard digital image techniques to extract the total projected area of the splash for 57-μm silicon carbide as a function of time (Fig. 3(a); [25]). Each curve represents the mean of three trial replicates; for clarity, error bars are not shown here (see Fig. S3 in Supplemental Material [25] for more details on trial-to-trial variation, which was small compared to variation with temperature). At room temperature $T = 25\,^{\circ}\mathrm{C}$ [black squares, Fig. 3(a)], the projected splash area rapidly increased, reached a maximum of $37.3\,\mathrm{mm}^2$ at 21.5 ms, then decreased gradually. As the temperature increased, the projected area of the splash decreased in maximum magnitude, and the time at which it reached the maximum also decreased. For example, at $T = 133\,^{\circ}\mathrm{C}$, the maximum area was $19.0\,\mathrm{mm}^2$ reached at 16.5 ms, while at the maximum temperature of 300 °C the maximum area was only $10.9\,\mathrm{mm}^2$ reached at 11.5 ms.

The above results were for silicon carbide granules of a particular size (57 μm). To test whether the splash suppression occurs with other types of granular media, we performed systematic tests with other sizes and chemical compositions (Advanced Abrasives, cf. Table I). In each case, qualitatively similar decreases in the granular splash were observed as the temperature increased. Figure 3(b) shows the mean projected maximum area observed for each media type, normalized on the mean maximum area observed at room temperature for that particulate type; Fig. 3(c) shows the "splash time" measured from impact ($t = 0$) until the time at which the maximum splash size was observed, again normalized on the corresponding splash time for room temperature. In each case, error bars are the standard deviation of three trial replicates. All seven tested types of granular media followed the same general decrease in maximum area and splash time, albeit with slightly different slopes. In general, the differences were insensitive to the three chemical compositions tested, with more variation depending on the particle size. The largest particulates tested had the smallest decrease in splash size and splash time, regardless of composition, while the smallest particulates had the largest decrease. These observations strongly indicate that the splash suppression at higher temperatures is a robust phenomenon.

III. EFFECT OF TEMPERATURE ON INTERPARTICLE FORCES

The experimental results in Figs. 1–3 clearly establish that the temperature of the granular media affects the splashing dynamics. The key question is why? One possible hypothesis is that the temperature alters the effective frictional forces between the particles. Indeed, a key observation is that the impactor penetrated to much smaller depths for higher temperatures [Fig. 4(a)]. Photographs from above after the splash clearly show that at room temperature the ball ended up completely immersed in the granular media, while at higher temperatures the penetration depth became increasingly smaller. At room temperature (25 °C), the ball was completely buried in the bed. Moreover, the apparent remains of a granular jet lay on top of the crater surface, presumably caused by the collapse of a deep granular cavity (cf. final image, top row of Fig. 3). For a moderate temperature impact (133 °C), the top of the ball was exposed and no granular jet was observed (cf. middle row Fig. 3). For a high-temperature impact (300 °C), the ball was most exposed and the top of the ball was occasionally higher than the bed surface. Since the ball landed with approximately the same kinetic energy regardless of the granular bed temperature, the decreased penetration suggests that the resistive force had increased with temperature.

One possibility for the weaker splashing and lesser penetration is that the temperature increased the frictional force between the granules. To test this hypothesis we systematically measured the "angle of repose" of the particles versus temperature. The repose angle of the material is related to the effective friction coefficient between particles such that $\mu_p = \tan\vartheta$, where θ is the steepest angle with respect to horizontal to which the granular media can be piled without slumping or sliding [27]. We measured the repose angle of our seven particle types, at both room temperature and following heating to 250 °C, using a fixed funnel method [Fig. 4(b)]. Specifically, we first heated a sample of the particles to more than 300 °C. Then the particles were poured into the funnel to create a granular

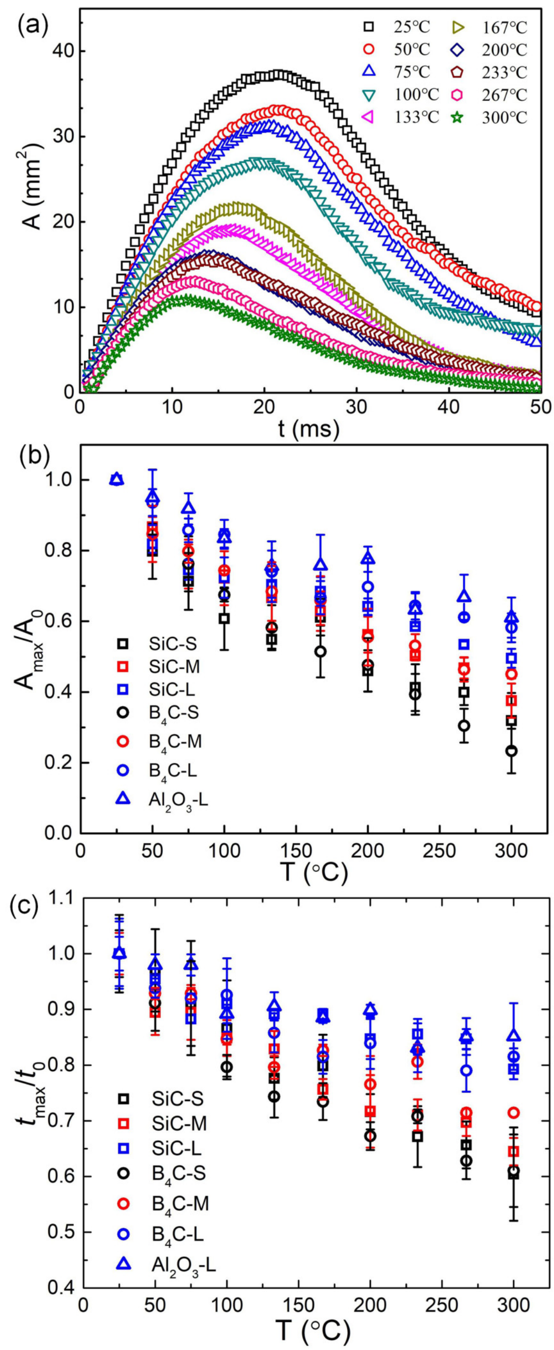

FIG. 3. Solid balls impact onto granular beds with varying temperature. (a) The time evolution of the splash projected area for 57-μm SiC particles ($\phi = 0.39$) for varying temperature. (b) The dimensionless maximum ejection area in each impact $A_{\max}/A_0$ for varying temperatures and granular materials. A_0 is the maximum splash area observed at room temperature. (c) The time that splash reaches its maximum area $t_{\max}$ vs T. In (b) and (c), the square, circle, and triangle represent SiC, B_4C, and Al_2O_3, respectively. The colors black, red, and blue represent the small (S), medium (M), and large (L) particle size, respectively. All data are averaged over three trial replicates; error bars are one standard deviation. The ambient gas is air.

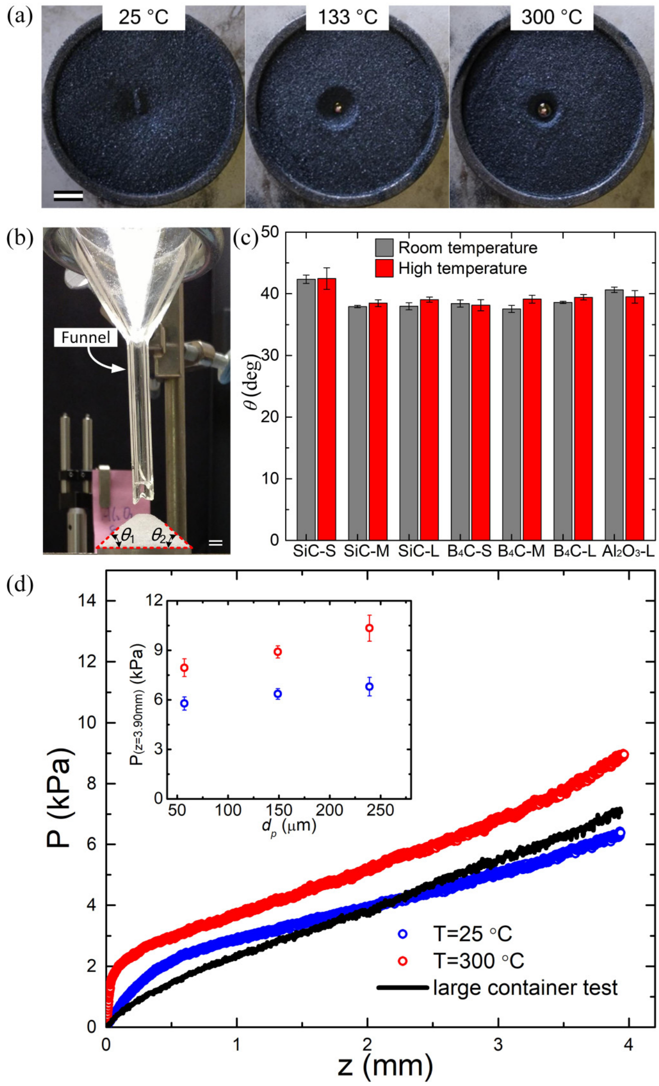

FIG. 4. The granular bed response under stress. (a) The crater after impact for $T = 25\,^{\circ}\mathrm{C}$, $133\,^{\circ}\mathrm{C}$, and $300\,^{\circ}\mathrm{C}$. The experiments are based on a SiC particle with $d_p = 57\,\mu\mathrm{m}$. The surrounding gas is air. Scale bar 5 mm. (b) The setup of funnel method used to measure the repose angle. Particles are Al_2O_3. Scale bar 5 mm. (c) The repose angle θ for varying materials at room temperature and high temperature (more than $250\,^{\circ}\mathrm{C}$). θ is the average value of the two angles (ϑ_1 and ϑ_2) measured in Fig. 4(b). The data are averaged over three trial replicates; the error bar is the standard deviation. (d) The stress P vs the stroke z for SiC particles with $d_p = 149\,\mu\mathrm{m}$. The blue and red circles represent $T = 25\,^{\circ}\mathrm{C}$ and $300\,^{\circ}\mathrm{C}$, respectively. The black line represents a special P-z test under room temperature with a large container which has an inner diameter of 213 mm and a depth of 10 mm. Each data point is obtained by the average of three independent runs. The inset shows the stress P at $z = 3.90$ mm for varying SiC particle size.

pile on an aluminum column (bottom diameter 35 mm). The aluminum column was itself put on another thermostatic heater and heated to $400\,^{\circ}\mathrm{C}$ to slow down the cooling of the granular pile. After that, the temperature of the granular pile was measured by infrared thermometer. The pouring process was conducted in less than 1 minute, so that the temperature was higher than $250\,^{\circ}\mathrm{C}$ in all tests. The observed variation of the repose angle θ was less than 3% between the room and high temperature [Fig. 4(c)], regardless of the particle type or size. We conclude the temperature had little effect on the friction coefficient μ_p.

A key difference between the angle of repose experiments and our splashing experiments, however, is that in our splashing experiments the particles were poured in cold and then heated. An alternative hypothesis, then, is that any change in volume upon heating (i.e., swelling with temperature) would cause "jamming" and necessarily increase the force necessary to displace the particles. Previous studies [28,29] on granular media have found that the thermal cycling can yield a more dense packing. In our study, in contrast, we only heat the granular bed once. After heating we observe that the height difference between the bed level and the container opening is very small, less than 0.4 mm, at 300 °C. This height increase roughly corresponds to a change in the packing fraction of less than 0.02 for the medium SiC particles, comparable to the deviation between trial replicates of three tests at room temperature (0.01, from 0.45 to 0.46). Moreover, the variation in the static stress at the same temperature but slightly different packing fractions is small compared to the differences observed at similar packing fraction but different temperatures. Thus the jamming happens even though loose packing the bed increases the packing fraction slightly.

Such heating-induced jamming has been investigated before in granular media [29], albeit not in the context of splashing. To test whether thermal expansion had any effect on the particles, we used a universal testing machine (Instron 5944) to measure the static strength of the granular bed. An aluminum pillar with a 5 mm diameter penetrated into the granular layer with a very low speed (1 mm/min), while the corresponding stress P was measured versus the displacement [Fig. 4(d)]. At room temperature, the stress versus displacement curve exhibited two distinct regimes: a relatively steep linear increase until approximately $z = 0.5$ mm, and then a transition to a less steep linear increase for the next several millimeters. In contrast, at 300 °C the stress increased extremely rapidly for the first 0.2 mm and then continued to increase linearly with a higher slope than for room temperature. Repeated tests with different particle sizes yielded qualitatively similar results. Choosing the final measured stress at $z = 3.90$ mm as a basis of comparison, it is clear that the overall stress was systematically larger by 37%–52% at the higher temperature [inset, Fig. 4(d)].

The P-z curves clearly have a steeper response regime in the shallow layer, followed by an asymptotic linear regime for P. The asymptotic linear regime in the "deep" layer is related to the hydrostatic pressure of the bed [30–32]. Katsuragi [30] interpreted the steeper response in the shallow layer as an elastic regime due to capillary bridging caused by adsorbed water moisture among grains. In our experiments, however, this apparent elastic regime for the 300 °C granular bed is much steeper than the room-temperature beds; at such high temperature any moisture should be evaporated and capillary bridging effects absent. Instead, it is worth noting that the elastic regime was much less pronounced in similar penetration stress experiments performed by Stone *et al.* [32]. The inner diameter of the container in Stone's tests (213 mm) was much larger than ours (31 mm) or Katsuragi's (30 mm). To test whether the container size mattered, we also tested the same particles inside a large container test (inner diameter 213 mm and depth 10 mm). The shallow elastic regime for this test is almost inconspicuous [black line in Fig. 4(b)], consistent with the observations by Stone. Thus we infer that the steep response of the elastic regime is induced by the proximity of the container sidewalls, which significantly amplify the force chains inside the bed. For the high-temperature bed, the thermal expansion effect could further enhance the force chains tied to the container walls, yielding the observed steeper response.

IV. EFFECT OF DIFFERENT AMBIENT GASES

Increasing the temperature not only affects the particles, it also affects the surrounding gas. Recall that, unlike liquids, in general increasing the temperature of a gas also increases its viscosity [33,34]. Thus a second potential hypothesis for the observed decrease in splashing is that the gas-phase viscosity significantly alters the splash dynamics.

TABLE II. The density ρ_g, the dynamic viscosity μ_g, and kinematic viscosity ν_g of the gas [34,35].

Gas	Air room	Air 300 °C	Ne	CO_2	SF_6
ρ_g (kg/m^3)	1.2	0.61	0.89	1.93	6.16
μ_g (μPa s)	18.3	29.3	31.3	14.7	16.1
ν_g (mm^2/s)	15.3	48.0	35.2	7.6	2.6

To test this hypothesis, and to decouple this effect from any possible heat-induced swelling of the particles, we performed experiments at room temperature but with gases of different composition. In this manner we systematically investigated how the gas-phase properties (viscosity and density) affected the granular ejecta in both the acceleration stage and the ballistic stage. The apparatus used here was broadly similar to the varying temperature tests, except that the heater was removed and the whole apparatus was placed inside of a sealed chamber that allowed the experiment to be conducted with ambient gases of different composition and pressure (Fig. S4 [25]). After preparing the bed (at room temperature), a vacuum was first applied to the chamber for 10 min, and then the specific gas was fed into the chamber until it reached a pressure of 1 atm. The pressure was held constant for at least 15 min before solid ball impact to ensure the system had equilibrated. An electronic hygrometer was used to monitor the temperature and humidity inside the chamber, which were maintained respectively at 25 °C ± 1 °C and less than 15%. Four kinds of gas were tested (cf. Table II): air, neon (Ne), carbon dioxide (CO_2), and sulfur hexafluoride (SF_6), chosen because they have a wide range of dynamic and kinematic viscosities. Depending on the gas, the Reynolds number of the falling ball ($\mathrm{Re}_b = \frac{\rho_g U_b D}{\mu_g}$) ranged from approximately 100 to 2100, where ρ_g and μ_g are the density and dynamic viscosity of the gas, respectively. Over this range, changes in the gas composition had no significant effect on the ball impact velocity (cf. Fig. S1b [25]).

The experiments with gases of different composition yielded qualitatively similar granular splashes as observed with air at room temperature, but the dynamics were quantitatively altered (Fig. 5). Representative results for the total projected area of the splash for 57-μm SiC are plotted in Fig. 5(a). Notably, for the three gases with the most similar dynamic viscosities (room-temperature air, CO_2, and SF_6), the time evolution of the projected splash area was most similar. In contrast, for the two gases with significantly higher dynamic viscosity (neon and high-temperature air), the rate of growth of the splash area was decreased in both the splash expansion stage and the dissipation stage. Again, tests with granules of different sizes showed that the influence of the gas composition was robust. The splash size $A_{\max}$ in different ambient gases and varying particle sizes is plotted in Fig. 5(b). The maximum magnitude of the projected area $A_{\max}$ for neon for the 57-μm particles was 46% smaller than that for sulfur hexafluoride (SF_6). The gap in splash size between Ne and SF_6 reduced gradually as the particle size was increased. For SiC with diameter $d_p = 239\,\mu$m, the variation between Ne and SF_6 test was only 7%. Statistical analysis using ANOVA (analysis of variance, performed using the "anova1" function in Matlab) to compare the maximum splash areas of the four different room-temperature gases indicates that the gas composition yielded statistically significant differences for $d_p = 57$ and 149 μm (yielding p values of 0.001 and 0.003, respectively) but not for $d_p = 239\,\mu$m (yielding a p value of 0.66). Figure 5(c) shows the corresponding splash times. In general, the splash time between gases with different dynamic viscosity exhibits a larger difference for the smallest particulates (57 μm). The difference was negligible for particulates with size $d_p = 239\,\mu$m.

To test whether other gas properties (such as gas density) affect the splash, we also performed experiments with reduced air pressure. Air was pumped out of the chamber until the air inside the chamber reached a target value (0.2–1.0 bar). Notably, in this pressure range the air viscosity is nearly constant [36]. The results (Fig. 6) show that $A_{\max}$ is insensitive to the air pressure for SiC beds with all the particle sizes used herein. Likewise, the characteristic splash time was insensitive

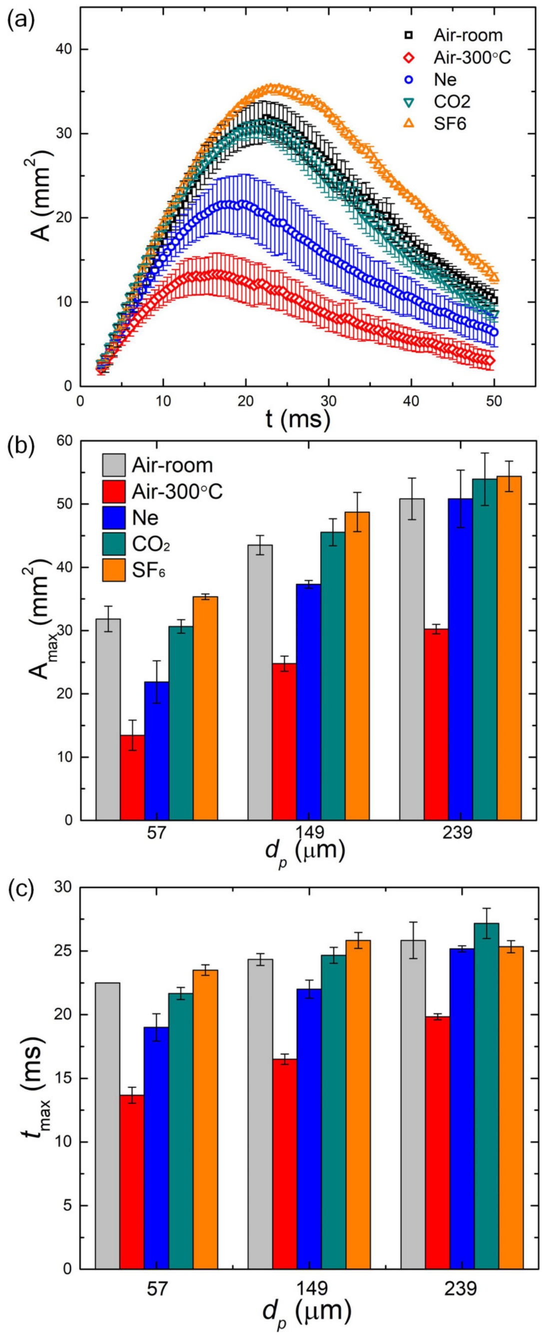

FIG. 5. The particle ejection after impact with varying surrounding gas. (a) The time evolution of the splash projected area for 57-μm SiC particles ($\phi = 0.39$) immersed in different gases. (b) The maximum ejection area for SiC with $d_p = 57$, 149, and 239 μm. (c) The time that splash reaches its maximum area $t_{\max}$ vs T. The legend in (c) is the same to (b). All data are averaged over three trial replicates; error bars are one standard deviation. The tests for room-temperature air, Ne, CO_2, and SF_6 were performed using the setup shown in the Supplemental Material, Fig. S4 [25], while the tests for 300 °C air were performed using the setup shown in Fig. 1. All imaging parameters (including focus length, resolution of camera, and the backlight intensity) were kept unchanged between tests.

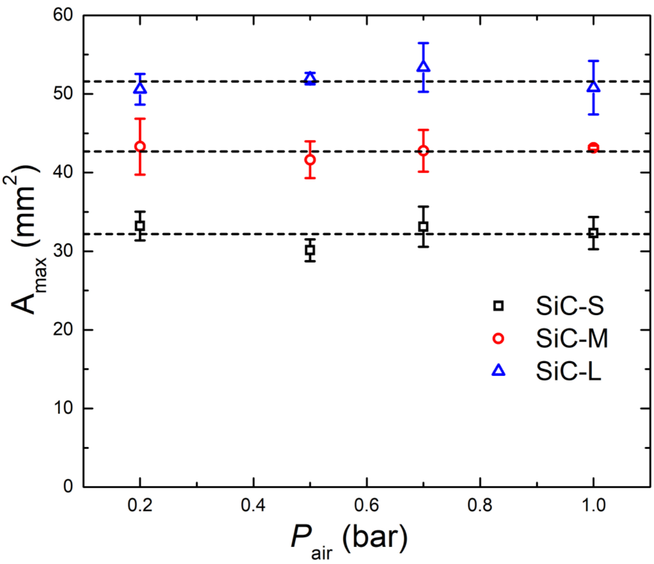

FIG. 6. Maximum projected areas of the granular splash in reduced air pressure. Particles were SiC of different sizes, immersed in air at varied pressure. Data are averaged over three trial replicates. Error bars are one standard deviation.

to the pressure (not shown). This result, coupled with the clear trends shown in Fig. 5, suggests that the gas viscosity, and not its pressure, most affect the splash dynamics.

If the gas viscosity affects the splashing, the next question is how it affects the splash. Specifically, the gas viscosity could play a role either in the particle acceleration stage upon impact, or the subsequent ballistic stage following ejection. To study the acceleration stage, we quantified the initial trajectories of the "fastest" particle among the ejecta, defined here as the first particulate to separate from the tip of the splash bulk at either the extreme left or right of the splash (cf. inset image in Fig. 7(a), and Fig. S5 [25]). These fastest particles were typically isolated and thus simplest to track with image analysis; they also were presumably least affected by many-body aerodynamic interactions with the other particles in the splash. The initial ejection velocity and ejection angle were averaged over three trial replicates (including both the left and right sides, so a total of six particles per experimental condition). For impacts on the smallest size particles ($d_p = 57\ \mu$m), the composition of the surrounding gas had little effect on the ejection angle or ejection velocity, on average near 40 degrees and approximately 0.9 m/s, respectively (Fig. S5 [25]). Similar results were found independent of the ambient air pressure. In other words, in our experiments the initial velocity and trajectories of the earliest splash ejecta following the impact were insensitive to the surrounding gas.

The subsequent behavior after the initial ejection, however, was strongly affected by the surrounding gas. Our observations of the entire ballistic trajectory of the ejecta indicate that the observed splash suppression is consistent with a pronounced viscosity dependence. By Newton's 2nd law, the time evolution of a particle trajectory obeys the system of equations

$$m\ddot{x} = -F_{dx}, \quad m\ddot{y} = -F_g - F_{dy}. \tag{1}$$

Here x and y represent the horizontal and vertical distance that a particle traveled, respectively, $\ddot{x}$ and $\ddot{y}$ are accelerations in the x and y directions, $F_g = \rho_p g \pi d_p^3/6$ is the gravitational force, and F_{dx} and F_{dy} are the component of the drag force along the x and y axes, respectively. The origin is defined here as the location where the particle first appears out of the bed surface, and the initial velocity is obtained as described above (cf. Fig. S5 [25]). If the flow is assumed to be inviscid with

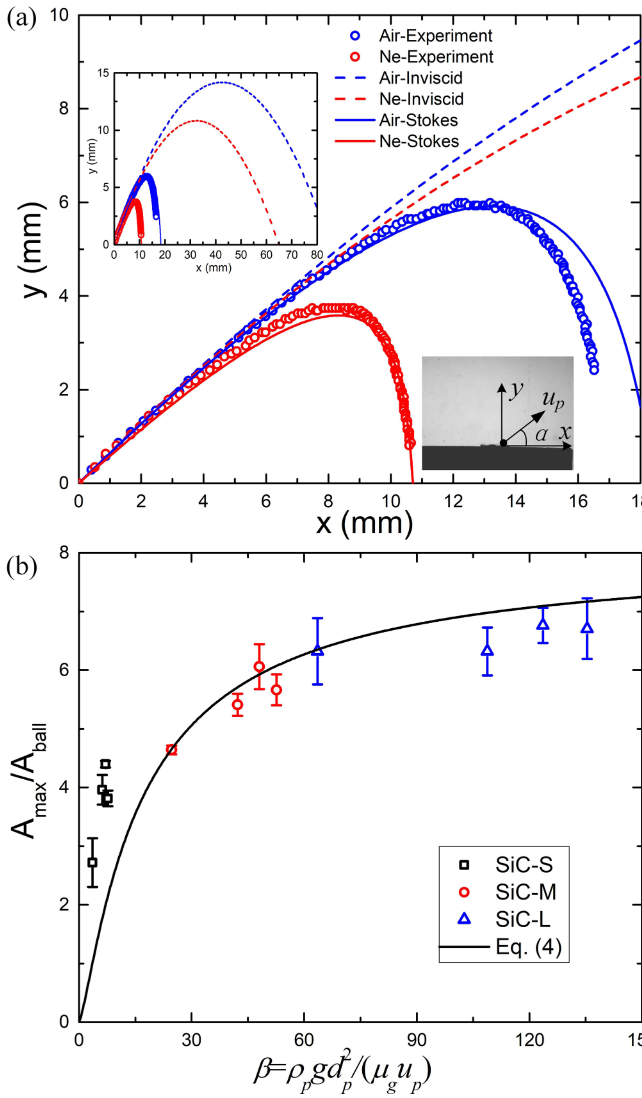

FIG. 7. Splash in varying gas environments. (a) Representative trajectories of the first particles ejected from the bed. The red and blue circles represent a case of impact in neon and air environment, respectively. The solid lines are the corresponding results calculated by Eq. (3) with initial speed u_p and ejection angle α measured by the experiments. The dashed lines are calculated assuming inviscid motion, Eq. (2). Impact in air: $u_p = 1.05\,\text{m/s}$, $\alpha = 33.1^\circ$. Impact in neon: $u_p = 0.89\,\text{m/s}$, $\alpha = 30.7^\circ$. Granular bed employed here is SiC with $d_p = 57\,\mu\text{m}$. (b) The maximum projected area of the splash A_{max} normalized by the projected area of the ball A_{ball} vs $\beta = F_g/F_d$. The color (black, red, and blue) of the box denotes three levels of particle size (S: 57, M: 149, and L: 239 μm) used herein. The data are averaged over three trial replicates, and error bars are one standard deviation. The solid line is the normalized projected area $A_{\text{max}}/A_{\text{ball}}$ calculated using Eq. (4), with the prefactor $\epsilon = 0.13$ found by regression using a Newton iteration.

$F_d = 0$, then Eq. (1) simplifies to the classic ballistic equations

$$x = u_p t \cos\alpha, \quad y = u_p\, t \sin\alpha - \frac{gt^2}{2}. \tag{2}$$

We measured representative trajectories of a SiC particle ($d_p = 57\ \mu$m) in room temperature air and in neon [Fig. 7(a)]. Comparison of the calculated inviscid trajectories, however, indicates that neglect of the drag yields a vast overestimate for how far the particulates should travel given their observed initial velocities and ejection angle [Fig. 7(a), dashed lines], with total horizontal displacements predicted to be approximately a factor of 6 larger than the actual observed displacements. We conclude that drag cannot be neglected.

To model this effect, note that drag force in general is $F_d = \frac{1}{8}C_d\pi\rho_g v_p^2 d_p^2$, where C_d is the drag coefficient and v_p is the instantaneous velocity of the particle. The Reynolds number at the initial moment of ejection is $\mathrm{Re}_i = \frac{\rho_g u_p d_p}{\mu_g}$. Using $u_p = 0.9\,\mathrm{m/s}$ as an estimate (cf. Fig. S5 [25]), the Reynolds number for the experiments reported here ranged from 1.4 to 82. In this range, the instantaneous coefficient of the drag force can be estimated by Rivkind's model [37] that $C_d = \frac{24}{\mathrm{Re}} + \frac{4}{\mathrm{Re}^{-1/3}}$, where $\mathrm{Re} = \frac{\rho_g v_p d_p}{\mu_g} \leqslant \mathrm{Re}_i$ is the instantaneous Reynolds number of the particle.

The first term of C_d is the Stokes' drag induced by viscous friction, while the second term is the inertial force applied by the gas flow, which is significant when Re $\gg$1. In Fig. 7(a), Re_i for air and neon are 3.4 and 1.4, respectively, so the inertial force term is insignificant. In other words, we approximate the drag force using Stokes' law here. In that situation, with the boundary condition that the initial velocity is u_p and ejection angle α as before, the particle trajectories can be estimated as

$$x = \frac{\rho_p d_p^2 u_p \cos\alpha}{18\mu_g}\left(1 - e^{-\frac{18\mu_g}{\rho_p d_p^2}t}\right),$$

$$y = \left(\frac{\rho_p d_p^2 u_p \sin\alpha}{18\mu_g} + \frac{\rho_p^2 d_p^4 g}{324\mu_g^2}\right)\left(1 - e^{-\frac{18\mu_g}{\rho_p d_p^2}t}\right) - \frac{\rho_p d_p^2 g}{18\mu_g}t. \tag{3}$$

Inclusion of the viscous drag yields excellent agreement with the observations [Fig. 7(a), solid lines]. Use of more complicated drag coefficient models, like Rivkind and Ryskin's model highlighted above [37], yielded only minor changes (not shown). Notably, in the reducing air pressure tests (cf. Fig. 6), the range of Re_i is 0.7–3.4, 1.8–8.8, and 2.8–14.1 for $d_p = 57$, 149, and 239 μm, respectively; where the viscosity remained constant but the gas density decreased significantly, the splash size varied little. This observation strongly implies the splash suppression is also dominated by the viscous force. Similarly, the splash in the three gases with most similar viscosity but larger difference in density exhibited similar splash sizes. We conclude that the effect of inertial force is weaker than the friction force term for the evolution of the splash in our study range. Note that some prior studies have focused on much higher impact velocities and correspondingly higher Reynolds numbers for their ejecta (e.g., the work by Marston *et al.* [14]).

To further test the role of the viscous forces on the splash in different kinds of granular beds, we define a dimensionless force $\beta = \frac{\rho_p g d_p^2}{\mu_g u_p} \sim \frac{F_g}{F_d}$ as the ratio of gravitational to viscous forces acting on the splash. A plot of the maximum splash area (normalized on the projected area of the ball) versus β shows a systematic increase and then a plateau; note that as β increases, the viscous force becomes smaller [Fig. 7(b)]. For $\beta > 60$ in Fig. 7(b), the gas viscous drag effect is relatively weak and the splash area is nearly independent of β. For smaller values of β, i.e., when the gas drag force is large, the splash area decreases in size.

We can use the ballistic trajectory of the fastest ejecta to derive a prediction for the maximum area of the splash. If we approximate all the granules as launched into motion with the same ejection angle $\alpha = 40^\circ$ and initial velocity $u_p = 0.9\,\mathrm{m/s}$, starting one ball diameter D_{ball} apart, from Eq. (3) we find that the individual granules reach their maximum height at $t_{\max} = -\frac{\beta u_p}{18g}\ln(\frac{\beta u_p}{18u_p\sin\alpha+\beta u_p})$. Since we only examine the projected view here, we do not need to consider smaller ejection angles or the ejection in the third dimension (into or out of the image plane). Assuming that all the following granules are similarly restrained to follow this trajectory, the total projected area of the splash will likewise reach its peak at $t_{\max}$. (This approach implicitly assumes that the first ejecta reaches their peak well before particles top ejecting from the bed, which is true for all splashes observed here, cf. Supplemental Material, Movie 1 [25].) The projected area of all the trajectories is then related to the spatial integral of the trajectory, $A_{\max} = D_{\text{ball}} y_{\max} + 2\int_0^{y_{\max}} x dy$, where D_{ball} is the diameter of the solid ball, and $y_{\max} = (\frac{u_p^2 \beta \sin\theta}{18g} + \frac{\beta^2 u_p^2}{324g})(1 - e^{-\frac{18g}{\beta u_p} t_{\max}}) - \frac{\beta u_p}{18} t_{\max}$ is the maximum height the particles reached. In reality, the particles in the splash are sparse, i.e., the particles do not completely fill the projected area of the splash. Therefore we insert an empirical "sparsity" prefactor ϵ, constrained as $0 < \epsilon < 1$, to account for the sparsity, yielding the predicted maximum splash size as

$$A_{\max} = \epsilon \left[D_{\text{ball}} y_{\max}(\beta) + 2 \int_0^{y_{\max}(\beta)} x(\beta) dy \right]. \tag{4}$$

This integral is readily integrated numerically, yielding the solid line in Fig. 7(b). The sparsity coefficient was found via regression (by Newton iteration), yielding $\epsilon = 0.13$, which is qualitatively consistent with the observed splashes. Importantly, Eq. (4) qualitatively follows the observed trends, increasing rapidly at low β and tapering off at high β. This result suggests that changes in the gas viscosity are sufficient to account for the observed variation in splash size for the different gases.

V. CONCLUSIONS

In summary, we provide systematic experiments establishing that the temperature strongly affects granular splashing. The thermal expansion of the granules enhances the force chain inside the granular beds, resisting penetration of the impactor and consequently diminishing the splash. The temperature also affects the gas viscosity and strongly affects the ballistic trajectories, and corresponding splash dynamics, for sufficiently small particles. In contrast to prior work, the air density was found to have little effect on both stages of splash evolution.

Several questions remain unanswered. We emphasize that our work here focused on initially loose granular beds at relatively low packing fractions; different results might be observed with more densely packed granular beds [21,38,39]. Likewise, all experiments conducted here involved grains that were poured in loosely, then heated; less temperature influence might be observed if the grains were first heated and then poured in loosely. Furthermore, the effect of deviations from monodispersity was not investigated here, although there is reason to believe the particle size distribution could affect the dynamics [20]. Future work would benefit from detailed assessments of these potential effects.

Despite these unanswered questions, the results do have several important implications. First, work to date on granular splashing has ignored the temperature; our results suggest that any experiments where processes that alter the temperature (such as pulling a vacuum or pressurizing a container) conceivably could serve as confounding factors. In terms of specific applications, sand and soil erosion rates might vary between night and day due to ambient temperature fluctuations. More dramatically at planetary scales, temperature in many planets undergoes much larger periodic changes: for example, Mars has temperature variations as large as of 120 °C from daytime to nighttime. The results provided here suggest that the ejecta patterns from meteorite strikes might depend sensitively on whether the strike occurred at nighttime or daytime. The results presented here suggest more detailed investigation of these hypotheses is warranted.

ACKNOWLEDGMENTS

This research has been supported by the National Key R&D Program of China (Grant No. 2018YFB2000903) and the National Natural Science Foundation of China (Grant No. 51875507).

[1] D. van der Meer, Impact on granular beds, Annu. Rev. Fluid Mech. **49**, 463 (2017).
[2] J. C. Ruiz-Suárez, Penetration of projectiles into granular targets, Rep. Prog. Phys. **76**, 066601 (2013).
[3] E. Grimaldi and E. Dressaire, Crater formation by sphere impact on a submerged granular bed, J. Visual. Jpn. **19**, 577 (2016).
[4] M. Fernández-Raga, C. Palencia, S. Keesstra, A. Jordán, R. Fraile, M. Angulo-Martínez, and A. Cerdà, Splash erosion: A review with unanswered questions, Earth Sci. Rev. **171**, 463 (2017).
[5] T. D. Ho, P. Dupont, A. Ould El Moctar, and A. Valance, Particle velocity distribution in saltation transport, Phys. Rev. E **85**, 052301 (2012).
[6] F. Pacheco-Vázquez, Ray Systems and Craters Generated by the Impact of Nonspherical Projectiles, Phys. Rev. Lett. **122**, 164501 (2019).
[7] T. Sabuwala, C. Butcher, G. Gioia, and P. Chakraborty, Ray Systems in Granular Cratering, Phys. Rev. Lett. **120**, 264501 (2018).
[8] K. R. Housen and K. A. Holsapple, Ejecta from impact craters, Icarus **211**, 856 (2011).
[9] K. A. Holsapple, The scaling of impact processes in planetary sciences, Annu. Rev. Earth Planet. Sci. **21**, 333 (1993).
[10] C. Josserand and S. T. Thoroddsen, Drop impact on a solid surface, Annu. Rev. Fluid Mech. **48**, 365 (2016).
[11] A. L. Yarin, Drop impact dynamics: Splashing, spreading, receding, bouncing, Annu. Rev. Fluid Mech. **38**, 159 (2006).
[12] S. Deboeuf, P. Gondret, and M. Rabaud, Dynamics of grain ejection by sphere impact on a granular bed, Phys. Rev. E **79**, 041306 (2009).
[13] J. F. Boudet, Y. Amarouchene, and H. Kellay, Dynamics of Impact Cratering in Shallow Sand Layers, Phys. Rev. Lett. **96**, 158001 (2006).
[14] J. O. Marston, E. Q. Li, and S. T. Thoroddsen, Evolution of fluid-like granular ejecta generated by sphere impact, J. Fluid Mech. **704**, 5 (2012).
[15] D. Lohse, R. Bergmann, R. Mikkelsen, C. Zeilstra, D. van der Meer, M. Versluis, K. van der Weele, M. van der Hoef, and H. Kuipers, Impact on Soft Sand: Void Collapse and Jet Formation, Phys. Rev. Lett., **93**, 198003 (2004).
[16] D. Lohse, R. Rauhe, R. Bergmann, and D. van der Meer, Creating a dry variety of quicksand, Nature (London) **432**, 689 (2004).
[17] H. Katsuragi and D. J. Durian, Unified force law for granular impact cratering, Nat. Phys. **3**, 420 (2007).
[18] M. Hou, Z. Peng, R. Liu, K. Lu, and C. K. Chan, Dynamics of a projectile penetrating in granular systems, Phys. Rev. E **72**, 062301 (2005).
[19] J. O. Marston, J. P. K. Seville, Y. Cheun, A. Ingram, S. P. Decent, and M. J. H. Simmons, Effect of packing fraction on granular jetting from solid sphere entry into aerated and fluidized beds, Phys. Fluids **20**, 023301 (2008).
[20] N. Kouraytem, S. T. Thoroddsen, and J. O. Marston, Penetration in bimodal, polydisperse granular material, Phys. Rev. E **94**, 052902 (2016).
[21] J. R. Royer, B. Conyers, E. I. Corwin, P. J. Eng, and H. M. Jaeger, The role of interstitial gas in determining the impact response of granular beds, EPL **93**, 28008 (2011).
[22] G. Caballero, R. Bergmann, D. van der Meer, A. Prosperetti, and D. Lohse, Role of Air in Granular Jet Formation, Phys. Rev. Lett. **99**, 018001 (2007).
[23] J. R. Royer, E. I. Corwin, P. J. Eng, and H. M. Jaeger, Gas-Mediated Impact Dynamics in Fine-Grained Granular Materials, Phys. Rev. Lett. **99**, 038003 (2007).
[24] J. R. Royer, E. I. Corwin, A. Flior, M. L. Cordero, M. L. Rivers, P. J. Eng, and H. M. Jaeger, Formation of granular jets observed by high-speed X-ray radiography, Nat. Phys. **1**, 164 (2005).
[25] See Supplemental Material at http://link.aps.org/supplemental/10.1103/PhysRevFluids.5.114302 for more detail on the impact velocity of the ball in Sec. S1, the image analysis of the splashes in Sec. S2, the area of the splash versus time for varied temperature in Fig. S3, the setup for the tests with gas of varied pressure or composition in Fig. S4, and the ejection velocity and angle of the first ejected particle in varying gas tests in Fig. S5.
[26] S. T. Thoroddsen and A. Q. Shen, Granular jets, Phys. Fluids **13**, 4 (2001).

[27] H. M. Beakawi Al-Hashemi and O. S. Baghabra Al-Amoudi, A review on the angle of repose of granular materials, Powder Technol. **330**, 397 (2018).
[28] K. Chen, J. Cole, C. Conger, J. Draskovic, M. Lohr, K. Klein, T. Scheidemantel, and P. Schiffer, Packing grains by thermal cycling, Nature (London) **442**, 257 (2006).
[29] W. L. Vargas and J. J. McCarthy, Thermal expansion effects and heat conduction in granular materials, Phys. Rev. E **76**, 041301 (2007).
[30] H. Katsuragi, Length and time scales of a liquid drop impact and penetration into a granular layer, J. Fluid Mech. **675**, 552 (2011).
[31] M. B. Stone, D. P. Bernstein, R. Barry, and M. D. Pelc, Getting to the bottom of a granular medium, Nature (London) **427**, 503 (2004).
[32] M. B. Stone, R. Barry, D. P. Bernstein, M. D. Pelc, Y. K. Tsui, and P. Schiffer, Local jamming via penetration of a granular medium, Phys. Rev. E **70**, 041301 (2004).
[33] J. C. Maxwell, XIII. The Bakerian Lecture.—On the viscosity or internal friction of air and other gases, Philos. Trans. Roy. Soc. **156**, 249 (1866).
[34] W. Sutherland, LII.The viscosity of gases and molecular force, Philos. Mag. **36**, 507 (1893).
[35] *CRC Handbook of Chemistry and Physics*, edited by D. R. Lide (CRC Press, Boca Raton, FL, 2004), p. 1188.
[36] J. Kestin and W. Leidenfrost, An absolute determination of viscosity of eleven gases over a range of pressure, Physica **25**, 1033 (1959).
[37] V. Y. Rivkind and G. M. Ryskin, Flow structure in motion of a spherical drop in a fluid medium at intermediate Reynolds numbers, Fluid. Dynam+ **11**, 5 (1977).
[38] H. Katsuragi, Morphology Scaling of Drop Impact onto a Granular Layer, Phys. Rev. Lett. **104**, 218001 (2010).
[39] J. O. Marston, S. T. Thoroddsen, W. K. Ng, and R. B. H. Tan, Experimental study of liquid drop impact onto a powder surface, Powder Technol. **203**, 223 (2010).